NANO · MICRO small
www.small-journal.com

Functionalized MoS_2 Nanovehicle with Near-Infrared Laser-Mediated Nitric Oxide Release and Photothermal Activities for Advanced Bacteria-Infected Wound Therapy

Qin Gao, Xiao Zhang, Wenyan Yin, Dongqing Ma, Changjian Xie, Lirong Zheng, Xinghua Dong, Linqiang Mei, Jie Yu, Chaozhan Wang,* Zhanjun Gu,* and Yuliang Zhao*

The rising dangers of bacterial infections have created an urgent need for the development of a new generation of antibacterial nanoagents and therapeutics. A new near-infrared 808 nm laser-mediated nitric oxide (NO)-releasing nanovehicle (MoS_2-BNN6) is reported through the simple assembly of α-cyclodextrin-modified MoS_2 nanosheets with a heat-sensitive NO donor *N*,*N*′-di-sec-butyl-*N*,*N*′-dinitroso-1,4-phenylenediamine (BNN6) for the rapid and effective treatment of three typical Gram-negative and Gram-positive bacteria (ampicillin-resistant *Escherichia coli*, heat-resistant *Escherichia faecalis*, and pathogen *Staphylococcus aureus*). This MoS_2-BNN6 nanovehicle has good biocompatibility and can be captured by bacteria to increase opportunities of NO diffusion to the bacterial surface. Once stimulated by 808 nm laser irradiation, the MoS_2-BNN6 nanovehicle not only exhibits photothermal therapy (PTT) efficacy but also can precisely control NO release, generating oxidative/nitrosative stress. The temperature-enhanced catalytic function of MoS_2 induced by 808 nm laser irradiation simultaneously accelerates the oxidation of glutathione. This acceleration disrupts the balance of antioxidants, ultimately resulting in significant DNA damage to the bacteria. Within 10 min, the MoS_2-BNN6 with enhanced PTT/NO synergetic antibacterial function achieves >97.2% inactivation of bacteria. The safe synergetic therapy strategy can also effectively repair wounds through the formation of collagen fibers and elimination of inflammation during tissue reconstruction.

1. Introduction

Bacterial infections cause intractable public health problems worldwide.[1,2] In particular, the indiscriminate use of antibiotics is leading to growing drug resistance in bacteria, resulting in life-threatening infections and an increasing economic burden.[3] The rising dangers of drug-resistant bacteria have created an urgent requirement for new antibacterial therapeutics and potent agents. In recent years, the rapid development of nanotechnology has highlighted some typical nanomaterials, such as noble metals, carbon, semiconductor metal sulfides/oxides, and polymer nanostructures, that offer opportunities for combating drug-resistant bacteria.[4–13] Near-infrared (NIR) laser-triggered photothermal therapy (PTT) based on various nanoagents has become one of the most effective antibacterial strategies due to the high spatial resolution and tissue penetration depth of NIR lasers.[14–16] Additionally, NIR lasers can be focused on a target area to promote blood circulation and relieve inflammation of tissues. However, there are still some limitations to PTT alone, whose antibacterial effect is restricted by the following issues: i) healthy tissue can be damaged by both high power density and long-term exposure to NIR lasers;[17] ii) heat-resistant bacteria are very difficult to kill even when treated at high temperatures for example 45 °C and some can survive at 60 °C for 30 min;[18] iii) single antibacterial strategies using nanoagents cannot rapidly and effectively eradicate bacteria because of the poor diffusivity of nanoagents compared with small-molecule drugs.[19] PTT-based synergistic therapy is a

Q. Gao, Dr. X. Zhang, Prof. W. Y. Yin, D. Q. Ma, Dr. C. J. Xie, Prof. L. R. Zheng, Dr. X. H. Dong, L. Q. Mei, Dr. J. Yu, Prof. Z. J. Gu, Prof. Y. L. Zhao
Key Laboratory for Biomedical Effects of Nanomaterials and Nanosafety
Institute of High Energy Physics and CAS Center for Excellence in Nanoscience National Center for Nanoscience and Technology of China
Chinese Academy of Sciences
Beijing 100049, China
E-mail: yinwy@ihep.ac.cn; zjgu@ihep.ac.cn

The ORCID identification number(s) for the author(s) of this article can be found under https://doi.org/10.1002/smll.201802290.

Q. Gao, Prof. C. Z. Wang
Key Laboratory of Synthetic and Natural Functional Molecule Chemistry of Ministry of Education
College of Chemistry and Material Science
Northwest University
Xi'an 710127, China
E-mail: czwang@nwu.edu.cn

Prof. Z. J. Gu, Prof. Y. L. Zhao
College of Materials Science and Optoelectronic Technology
University of Chinese Academy of Sciences
Beijing 100049, China

DOI: 10.1002/smll.201802290

promising strategy for addressing these limitations that integrates the advantages of single modality approaches to shorten antibacterial time and improve antibacterial efficiency as well as reduce the dose of antibacterial agents.[14,15,20] Moreover, most reported nanomaterials cannot simultaneously provide a simple synthesis process, good biocompatibility, high antibacterial activity, and effective promotion of bacteria-infected wound healing. It is therefore important to explore novel nanomaterials with multiple antibacterial functions.

Nitric oxide (NO), a typical lipophilic biological signal molecule, is a broad-spectrum antibacterial candidate, whose antibacterial process is not dependent on the type of bacteria, in contrast to traditional antibiotics.[21] NO plays a key role in the natural immune system response to infection based on its reducing power and its byproducts dinitrogen trioxide (N_2O_3) and peroxynitrite ($ONOO^-$), resulting in lipid peroxidation, rupture of bacterial cell membranes, and DNA deamination.[22] More importantly, unlike antibiotics, NO also promotes wound healing by increasing myofibroblast and collagen production during skin reconstruction.[23] We therefore believe that NO will improve the therapeutic effects and reduce side effects if incorporated into PTT for the treatment of bacteria. Although NO is a useful antibacterial agent, its antibacterial application is hindered by its short half-life and the lack of suitable vehicles for NO storage and delivery.[20] Previous reports have explored small-molecule NO donors as antibacterial agents by modulating exogenous stimuli such as light, pH, enzymes, and heat.[24–28] Other innovative nanovehicles have demonstrated potential for storage and controlled release of bactericidal quantities of NO at a designated site without undesired release.[29,30] Based on the antibacterial potential of NO and the design requirements of controlled-release NO nanovehicles, we envisaged that combination of a distinctive NIR laser-mediated NO donor with PTT could achieve promising antibacterial effects. In particular, nano-sized molybdenum sulfide (MoS_2), one of the new rising 2D transition metal dichalcogenides (TMDs),[31] is being investigated for biomedical applications, particularly as a nanocarrier and photothermal nanoagent, owing to its advantages such as large surface area, easy surface modification, and high NIR photothermal conversion property.[32–36] To date, although there are some concerns related to antibacterial applications of MoS_2, utilizing the high NIR photothermal effect and unique surface characteristics of MoS_2 for constructing highly effective antibacterial platforms is still in its infancy.[37,38] In particular, NIR light show low phototoxicity compared with short-wavelength such as UV or blue light. Therefore, we anticipate that smart design of NIR laser-mediated MoS_2 nanovehicles which integrate PTT and a photothermally sensitive NO donor into one system. The nanovehicle may make up for deficiencies of PTT or NO alone. If the nanovehicle can be well captured by bacteria, the system will improve NO delivery by enhancing the diffusivity of NO to bacterial surfaces through the accurate control of NO release.[39,40] The extra reactive nitrogen species (RNS) produced by NO can damage the cell membranes of bacteria,[24] which then show enhanced permeability and sensitivity to heat,[41] consequently inducing significant DNA damage to make bacteria more vulnerable.

Here, we report a versatile MoS_2-BNN6 nanovehicle for 808 nm laser-mediated NO release through simple assembly of α-cyclodextrin (α-CD) modified MoS_2 nanosheets (MoS_2-α-CD) with a heat-sensitive NO donor *N,N′*-di-sec-butyl-*N,N′*-dinitroso-1,4-phenylenediamine (BNN6) for safe, rapid, and effective disinfection of inflammatory wounds (**Scheme 1**A–D). When captured by bacteria, MoS_2-BNN6 can increase opportunities for the diffusion of NO to the bacteria surface. Once stimulated by an 808 nm laser, hyperthermia from MoS_2-BNN6 can precisely control NO delivery and on-demand release. Simultaneously, MoS_2 induced hyperthermia under 808 nm irradiation can accelerate oxidation of antioxidant glutathione (GSH) into its disulfide (GSSG), which disrupts balance of antioxidants in the bacteria. Consequently, NO released from MoS_2-BNN6 interacts with bacteria and can induce oxidative/nitrosative stress-oriented DNA damage (Scheme 1E). The PTT/NO synergetic antibacterial strategy achieved higher inactivation of bacteria within 10 min compared with PTT alone. In particular, wound therapy demonstrates that this strategy can effectively repair wounds through the formation of collagen fibers and elimination inflammation. This work proposes a low-cost MoS_2-BNN6 antibacterial agent that has significant potential therapeutic effects on clinical drug-resistant and heat-resistant bacteria-infected wounds.

2. Results and Discussion

Layerd TMDs, such as MoS_2 nanosheets, commonly have hydrophobic surface. And α-CD, with a hydrophobic inner cavity and a hydrophilic exterior, has potential as a stabilizer for modifying MoS_2 nanosheets. Herein, the MoS_2 nanosheets were synthesized according to a modified method previously reported by our group.[42] Then, the MoS_2 nanosheets were simply functionalized with α-CD at room temperature, leading to a high loading of BNN6 through hydrophobic interactions of MoS_2 surface, α-CD, and BNN6 (Scheme 1A).

Field emission scanning electron microscopy (FE-SEM) (Figure S1, Supporting Information) and transmission electron microscopy (TEM) (**Figure 1**A) showed that the size of MoS_2 nanosheet was ≈50–80 nm with sheet-like morphology. Atomic force microscopy (AFM) images indicated that the height of MoS_2-α-CD (Figure S2, Supporting Information) increased to ≈1.2 nm compared with the nude single-layer MoS_2 nanosheets (≈0.6 nm) (Figure 1B), implying the successful attachment of α-CD to both planes of the nanosheets. Raman spectra (Figure 1C) demonstrated that both nude MoS_2 and MoS_2-α-CD exhibit two distinct band features corresponding to typical 2H phase.[43,44] X-ray photoelectron spectroscopy (XPS) further supported the successful synthesis of MoS_2-α-CD nanosheets (Figure S3, Supporting Information). The hydrodynamic size of the MoS_2-α-CD nanosheets was about 181 nm, which was a little bigger than that of the MoS_2 nanosheets (≈133 nm) (Figure S4A,B, Supporting Information). The loading ratio of α-CD was calculated to be about 30% through thermal gravimetric analysis (TGA) (Figure S5A, Supporting Information). In addition, both MoS_2 and MoS_2-α-CD nanosheets exhibited good stability in phosphate buffered saline (PBS) over 24 h (Figure S5B,C, Supporting Information), which is beneficial for the effective capture of MoS_2-BNN6 by bacteria, thereby increasing the contact area and diffusion opportunities for NO

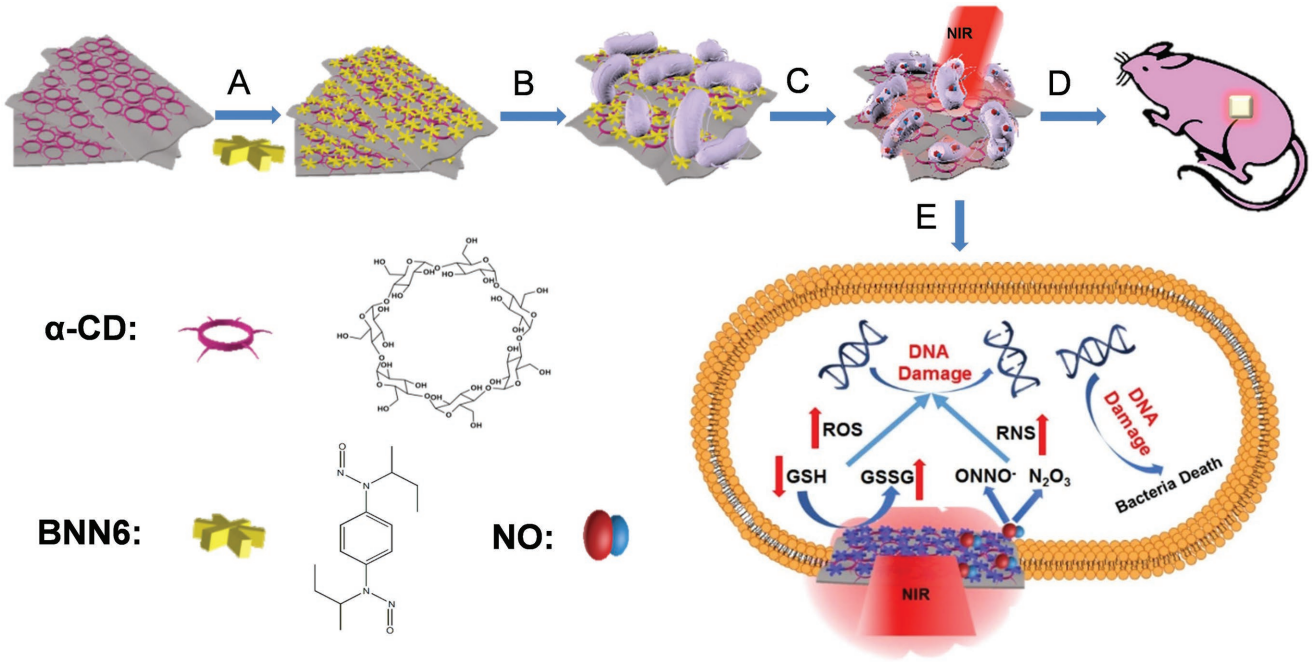

Scheme 1. Schematic illustration of MoS_2-BNN6 as NIR laser-mediated NO release nanovehicle for synergistic eliminating bacteria. A) α-CD modified MoS_2 (MoS_2-α-CD) assembly with BNN6 to form MoS_2-BNN6 through a simple hydrophobic interaction. B) MoS_2-BNN6 was captured by bacteria. C) 808 nm laser irradiation induced NO release improves bactericidal efficiency by synergetic PTT/NO. D) MoS_2-BNN6 used in wound disinfection and healing. E) The antibacterial principle based on synergetic PTT/NO for elevating ROS/RNS while reducing GSH level. The ROS/RNS could interact with DNA to induce oxidative/nitrosative stress, ultimately disrupting vital cellular functions and structures, leading to rapid and enhanced antimicrobial efficacy.

to the bacteria (Scheme 1B). Next, the NO donor BNN6 was loaded on the surface of MoS_2-α-CD through the host–guest interaction between α-CD and BNN6 molecules (Figure S6, Supporting Information). The success of loading was verified by Fourier transform infrared (FT-IR) spectra. As shown in Figure 1D, the as-prepared MoS_2-α-CD exhibited a similar spectrum to that of α-CD while the MoS_2-BNN6 exhibited similar spectrum to that of BNN6. The peaks at 3430 and 1640 cm^{-1} can be assigned to the stretching of —OH, and the bands from 1000 to 1200 cm^{-1} resulted from skeletal vibrations of C—O—C stretching.[45] These groups were attributed to α-CD. Additionally, the peak at 1377 cm^{-1} referred to the deformation of N—N=O, indicating the successful loading of BNN6. UV–vis–NIR spectra of the MoS_2-α-CD before and after loading with BNN6 showed broad absorption from 200 to 900 nm compared with the absorption peaks of α-CD and BNN6. In particular, the UV–vis–NIR spectrum of MoS_2-BNN6 showed an additional absorption peak about 250 nm, which was not present for MoS_2-α-CD, further suggesting the effective loading of BNN6 onto the MoS_2-α-CD nanosheets (Figure 1E). The BNN6 loading ratio was concentration dependent with a saturation loading capacity of 42% (Figure 1F) calculated from the standard curve of BNN6 (Figure S7, Supporting Information).

As reported, the long-wavelength 808 nm NIR light has a high penetration depth into tissues and a low phototoxicity compared with short-wavelength such as UV light. The nanosized MoS_2 also has high NIR photothermal conversion ability.[15] In our experiments, the photothermal effect of MoS_2-α-CD was measured under 808 nm laser irradiation (1.0 W cm^{-2}) over 600 s. As shown in Figure 1G, the temperature clearly rose with increasing concentration of the MoS_2-α-CD aqueous suspension, suggesting its high photothermal conversion efficiency and significant potential as an NIR photothermally mediated nanovehicle for BNN6. Moreover, to verify the controlled NO release from MoS_2-BNN6 at different power densities of the 808 nm laser, the NO release profiles were quantitatively detected using a 2,3-diaminonapththalene (DAN) fluorescent probe with an emission wavelength of 405 nm (Figure 1H). Compared with the BNN6 group, NO released from MoS_2-BNN6 increased consistently with increasing power density over 30 min. This result suggests that the hyperthermia induced by MoS_2-BNN6 exposed to 808 nm laser irradiation plays an important role in the NO release, which largely improves the decomposition efficiency of BNN6. The decomposition process is shown in Figure S8 in the Supporting Information. In addition, 808 nm laser induced hyperthermia for NO release from MoS_2-BNN6 was compared with the result of direct heating (Figure 1I). It was found that the temperature increased to 53.3 °C after irradiation for 20 min (200 μg mL^{-1}, 1.0 W cm^{-2}) and the amount of NO released from MoS_2-BNN6 reached 4.5×10^{-6} M, while direct heating at 50 °C did not induce obvious NO release from MoS_2-BNN6. It has been reported that the surface temperature of nanomaterials is significantly higher than the average temperature of nanomaterials in a dispersion medium.[46] MoS_2-BNN6 therefore becomes a highly localized heat source, and the hyperthermia produced by the surface of MoS_2-BNN6 would therefore be higher than 53.3 °C, consequently benefiting the decomposition of BNN6. It is clear that

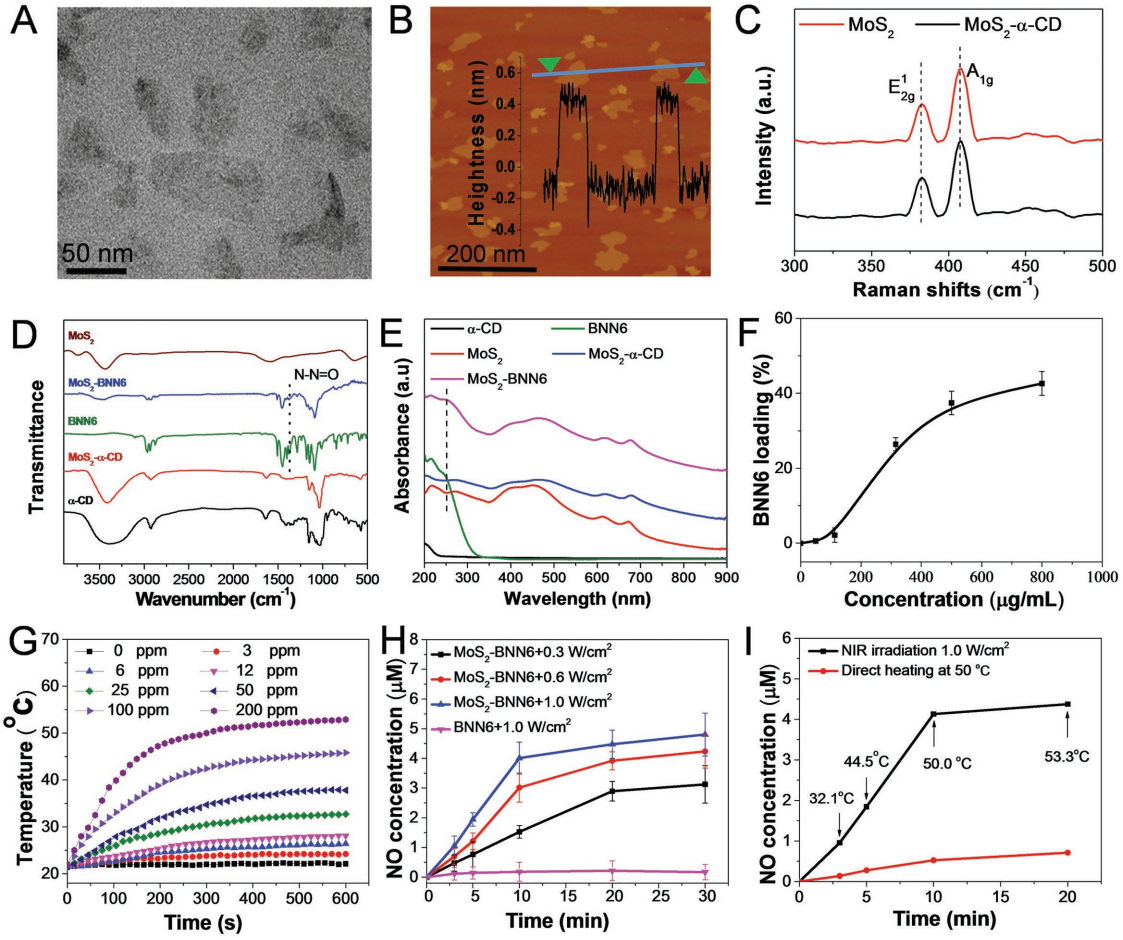

Figure 1. A) TEM and B) AFM images of single-layer MoS_2 nanosheets. C) Raman spectra of MoS_2 and MoS_2-α-CD nanosheets. D) FT-IR spectra of MoS_2, MoS_2-α-CD before and after loading with BNN6. E) UV–vis–NIR spectra of MoS_2, MoS_2-α-CD before and after loading with BNN6. F) Plots of loading percentage of BNN6 on MoS_2-α-CD. G) Photothermal effect of MoS_2-α-CD with different concentrations irradiated by 808 nm laser. H) NO release curves of MoS_2-BNN6 under varying power densities irradiation of 808 nm laser. I) Effects of direct heating and 808 nm laser irradiation on NO release from MoS_2-BNN6.

this multifunctional MoS_2-BNN6 nanovehicle has the ability to hold large payloads of BNN6 as well as to exhibit NIR-activated, spatiotemporal controlled NO release.

Next, the kinetics of NO released from MoS_2-BNN6 were monitored using a NO electrode (ISO-NOP, World Precision Instruments). As shown in Figure S9 and Table S1 in the Supporting Information, the as-prepared MoS_2-BNN6 had two NO release models: i) NIR-triggered NO release in a short time and ii) spontaneous release in a long time. With NIR laser irradiation, NO released rapidly from MoS_2-BNN6 due to the local heat effect on the surface of MoS_2 and then accumulated to a higher concentration. The concentration of NO could reach the level of μM, which can effectively inhibit bacteria when combined with PTT. After NIR irradiation, the concentration of released NO kept at a relatively low level (less than 500×10^{-9} M). We also measured the release behavior of MoS_2-BNN6 without NIR irradiation. The release profile was quite different from MoS_2-BNN6 after NIR irradiation. Therefore, we speculated that the heat might cause BNN6 desorption from MoS_2 nanosheets, and sequentially a minority of BNN6 began to release NO spontaneously. This is a very favorable phenomenon for wound healing because high concentration of NO could provide potential antibacterial ability at the early stage and low concentration of NO happens to meet the requirement of stimulating angiogenesis and new tissue formation in the middle and late period.

Encouraged by the above results, the synergetic PTT/NO bactericidal efficacy based on MoS_2-BNN6 nanovehicles toward Gram-negative ampicillin resistant *Escherichia coli* (Amp^r *E. coli*), Gram-positive heat-resistant *Escherichia faecalis* (*E. faecalis*), and Gram-positive *Staphylococcus aureus* (*S. aureus*) bacterial strains was evaluated using a plate count method. In **Figure 2** and Figure S10 in the Supporting Information, the number of colonies for the MoS_2-α-CD (200 μg mL^{-1}) + NIR treated group obviously decreased compared with the MoS_2-α-CD, BNN6 (80 μg mL^{-1}), and MoS_2-BNN6 (with equivalent BNN6) without 808 nm laser irradiation groups (Figure 2A,C and Figure S10A, Supporting Information). The inactivation of bacteria of the MoS_2-α-CD (200 μg mL^{-1}) + NIR treated group reached 55.9%, 73.2%, and 53.1% for Amp^r *E. coli*, *E. faecalis*, and *S. aureus*, respectively, after a 10 min of incubation followed by 10 min of irradiation (Figure 2B,D and Figure S10B, Supporting

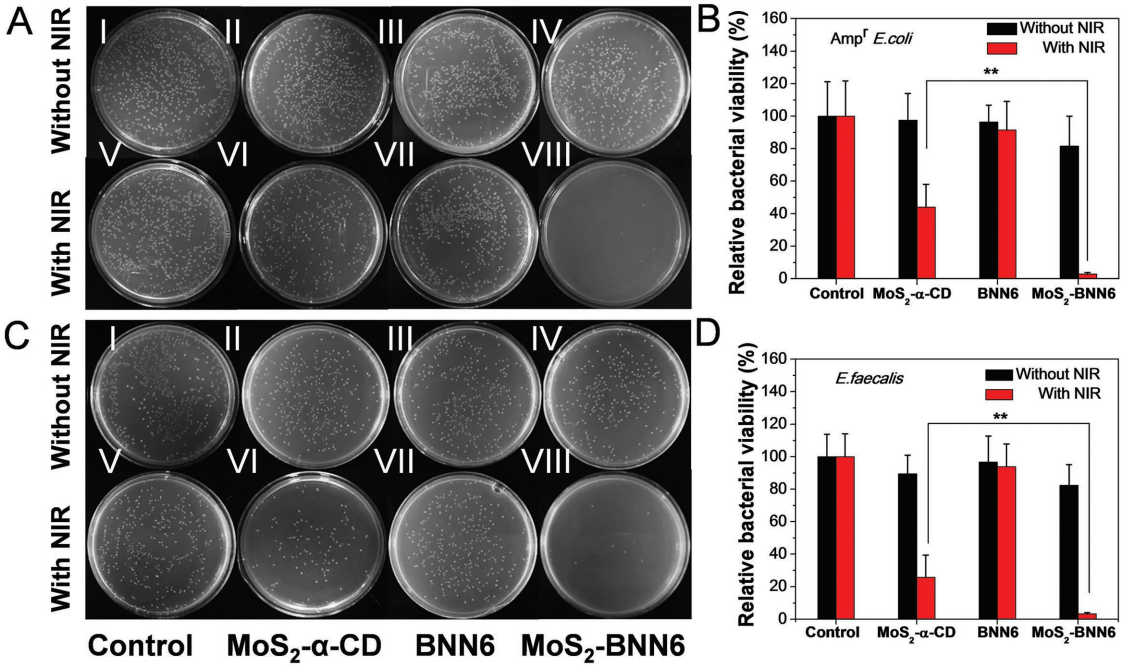

Figure 2. Photographs of bacterial colonies formed by A) Amp^r *E. coli* and C) *E. faecalis* treated with (I) PBS, (II) MoS_2-α-CD, (III) BNN6, (IV) MoS_2-BNN6, (V) PBS + NIR, (VI) MoS_2-α-CD + NIR, (VII) BNN6 + NIR and (VIII) MoS_2-BNN6 + NIR based on plate count method (concentration: [MoS_2] = 200 μg mL^{-1}, [BNN6] = 80 μg mL^{-1}). The corresponding bacterial viabilities of B) Amp^r*E. coli*, D) *E. faecalis* treated with PBS, MoS_2-α-CD, BNN6, and MoS_2-BNN6 without or with 808 nm laser irradiation (1.0 W cm^{-2}, 10 min), measured using plate count method.

Information). The MoS_2-BNN6 + NIR treated group exhibited high antibacterial activity against Amp^r *E. coli* (Figure 2A,B), *E. faecalis* (Figure 2C,D), and even pathogens such as *S. aureus* (Figure S10, Supporting Information). The inactivation of bacteria in the MoS_2-BNN6 + NIR treated group quickly reached 98.9%, 98.0%, and 97.2% for Amp^r *E. coli*, *E. faecalis*, and *S. aureus*, respectively. Furthermore, in the tested dose range, BNN6, MoS_2-α-CD, and MoS_2-BNN6 without NIR laser irradiation showed no clear antibacterial activity toward Amp^r *E. coli* (Figure S11, Supporting Information). However, the Amp^r *E. coli* inhibition rate evidently increased with increasing concentration of MoS_2-α-CD and MoS_2-BNN6 when exposed to 808 nm laser irradiation (Figure S12, Supporting Information). Meanwhile, the antibacterial activity of the PTT/NO synergetic system against nonresistant *E. coli* was also examined, and the inactivation rate rapidly increased to 99.0% after 10 min of 808 nm laser irradiation (Figure S13, Supporting Information). *E. faecalis* is linked with a wide range of human infections and is heat resistant.[47] We investigated whether external heating in a water bath at 50 °C (the same temperature as that of the NIR laser induced PTT experiment) for 12 h could eliminate *E. faecalis* (Figure S14, Supporting Information). Compared with the control group, there was no obvious death in the MoS_2-α-CD- or MoS_2-BNN6-treated *E. faecalis* at 50 °C in water bath. These results further revealed that *E. faecalis* cannot be efficiently killed by MoS_2-BNN6 + heat from a water bath (Figure S14, Supporting Information) or MoS_2-α-CD + NIR (Figure 2). Thus, a plausible reason for the effective killing of heat-resistant *E. faecalis* could be ascribed to hyperthermia at the MoS_2-BNN6 surface with synergetic NO therapy under NIR laser irradiation.

To further understand the antibacterial effect described above, the changes in the morphologies of Amp^r *E. coli* and *E. faecalis* were investigated using FE-SEM (**Figure 3**A). Amp^r *E. coli* had a smooth surface and a rod-like shape when treated with (I) PBS, (II) MoS_2-α-CD, (III) BNN6, (V) PBS + NIR, and (VII) BNN6 + NIR. Only a small amount of disruption appeared at the cell membranes of Amp^r *E. coli* after treatment with (IV) MoS_2-BNN6, suggesting that MoS_2-BNN6 alone had a minor impact on the integrity of the bacterial cell membranes. In contrast, Amp^r *E. coli* exposed to (VI) MoS_2-α-CD + 808 nm laser irradiation had incomplete and rough cell membranes (Figure 3A). After 10 min of treatment with (VIII) MoS_2-BNN6 followed by 10 min of NIR laser irradiation, the majority of the bacterial surfaces were torn and badly damaged, implying that the synergistic antibacterial strategy has potent antimicrobial properties. The cell death of *E. faecalis* after treatment in the PTT/NO group (VIII) was also very clear, with the cell membranes of *E. faecalis* having lost the normal structure. Consequently, it can be concluded that the synergetic antibacterial strategy based on NIR photothermally responsive MoS_2-BNN6 can perturb and damage cell membranes structure for rapid and highly effective killing of Amp^r *E. coli* and *E. faecalis*.

The disruption of Amp^r *E. coli* and *E. faecalis* by MoS_2-BNN6 + NIR was further demonstrated using green fluorescent nucleic acid dye (SYTO-9) and red fluorescent propidium iodide (PI) nucleic acids stains. SYTO-9 is membrane permeant, while PI penetrates only bacteria with damaged cell membranes.[48] The fluorescence images clearly show that both Amp^r *E. coli* and *E. faecalis* treated with MoS_2-BNN6 + NIR showed the most serious damage to the cell membranes compared with other groups (**Figure 4**A,B).

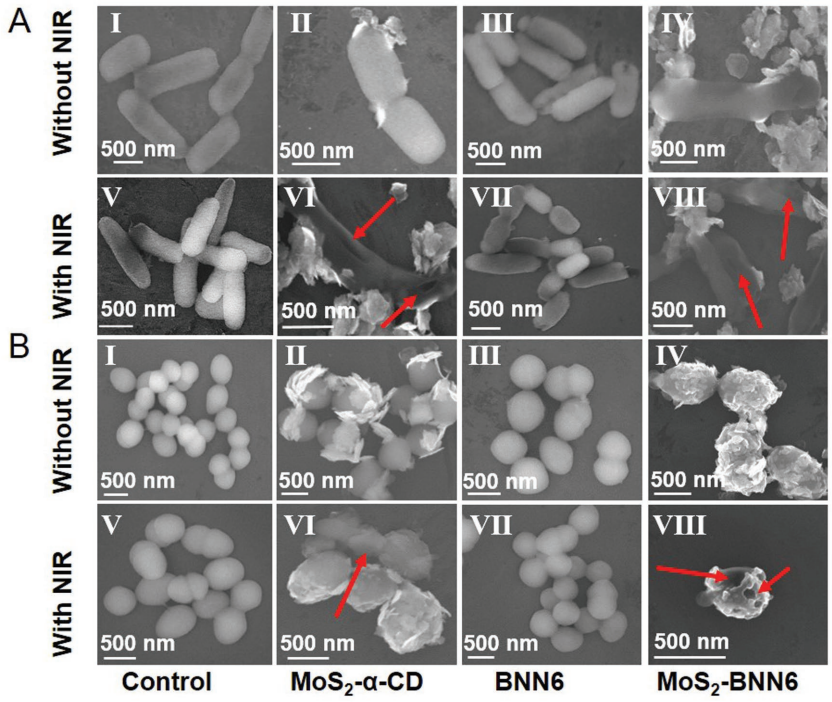

Figure 3. FE-SEM images of A) Amp^r *E. coli* and B) *E. faecalis* incubated with (I) PBS, (II) MoS_2-α-CD, (III) BNN6, (IV) MoS_2-BNN6, (V) PBS + NIR, (VI) MoS_2-α-CD + NIR, (VII) BNN6 + NIR, and (VIII) MoS_2-BNN6 + NIR. (1.0 W cm^{-2}, 10 min) (concentration: [MoS_2] = 200 μg mL^{-1}, [BNN6] = 80 μg mL^{-1}). Red arrows marked the broken sites of bacteria.

These results indicate that the bacterial membranes severely collapsed following synergistic PTT/NO treatment.

Oxidative stress plays a major role in nanomaterial-mediated antibacterial systems. For this antibacterial strategy, it is important to understand whether reactive oxygen species (ROS)-dependent oxidative stress will occur. First, we employed an ROS probe, 2,7-dichlorodihydrofluorescein diacetate (DCFH-DA), to monitor the formation of ROS induced by MoS_2-BNN6 exposed to 808 nm laser irradiation. In the presence of ROS, the DCFH-DA is oxidized to dichlorofluorescein,[49] which emits fluorescence when excited at 488 nm. As shown in **Figure 5**A, the result demonstrates that synergetic PTT/NO triggers more ROS production in bacteria compared with other groups. In addition to the production of ROS during the synergetic PTT/NO process, the scavenging ability of bacteria for ROS will also affect their activity. GSH is an important antioxidant present at high levels in many bacteria and can be oxidized into GSSG in the presence of radicals.[50–52] If the antioxidant defense of the bacteria is inhibited by oxidation of GSH into GSSG, the concentration of available radicals increases. Therefore, we evaluated the GSH level using Ellman's assay to determine the changes of GSH induced by MoS_2-α-CD with/without NIR laser irradiation. Typically, when MoS_2-α-CD is incubated with GSH, the GSH exhibits temperature-dependent and time-dependent oxidation behavior, which is intuitively demonstrated by tracing the color changes of the solutions (Figure 5C–E). Compared with the water bath group treated at 50 °C, a much higher GSH loss rate could be observed following treatment with MoS_2-α-CD and 808 nm laser irradiation (Figure S15, Supporting Information). Furthermore, the change of intracellular GSH was evaluated using a fluorescent probe *o*-phthaldialdehyde (OPA).[53] The reduced fluorescence at 420 nm in Figure 5B demonstrated that the GSH level in Amp^r *E. coli* decreased after incubation with MoS_2-α-CD with/without laser irradiation compared with untreated Amp^r *E. coli*. XPS spectra (**Figure 6**A) and X-ray absorption near-edge structure (XANES) spectra (Figure 6B) were used to confirm the chemical nature of Mo in MoS_2-α-CD under laser irradiation with/without GSH. The result shows that the composition and state of MoS_2 were unchanged during the above-described process. Therefore, MoS_2 could catalyze the oxidation of organic thiols (–SH) to produce disulfides (–S–S–) and the process of catalytic oxidation was temperature related.[52,54] The intracellular ROS production and depletion of GSH levels indicate that ROS induced oxidative stress could partly contribute to the antimicrobial action of the MoS_2-BNN6.

Furthermore, an NO-sensitive fluorescent probe 3-amino,4-aminomethyl-2′,7′-difluorescein, diacetate (DAF-FM DA) was used to determine whether the interaction between MoS_2-BNN6 + NIR and Amp^r *E. coli* could lead to more efficient delivery of NO to bacterial cells. In the presence of NO, DAF-FM DA can be oxidized/nitrosated by the byproducts of NO, which are RNS, resulting in bright green fluorescence due to generation of benzotriazole derivatives.[24,55] Figure 6C shows that Amp^r *E. coli* treated with DAF-FM DA and MoS_2-BNN6 + NIR exhibited strong green fluorescence, indicative of the successful release of NO in close proximity to bacterial cells, compared with other groups. Comet assay was performed to evaluate the MoS_2-BNN6 + NIR laser induced DNA damage.[56,57] **Figure 7**A shows that there were almost no stain tails observed for Amp^r *E. coli* incubated with MoS_2-α-CD, BNN6, MoS_2-BNN6, or BNN6 + NIR, implying negligible DNA damage resulting from these treatments. In marked contrast, for the PTT-treated samples, there was a clear presence of stain tails, which could be caused by hyperthermia-induced ROS from MoS_2-α-CD + NIR. However, the MoS_2-BNN6 + NIR group clearly gave rise to the longest stain tails, indicating the most effective damage to DNA. Given that the migration length is correlated with the fragment size and level of strand breaks, the high degree of DNA fragmentation indicated strand breaks of the cell nuclei in Amp^r *E. coli*, as suggested by all of the analyzed parameters (Figure 7B–E). Compared with other groups, the MoS_2-BNN6 + NIR group demonstrated the highest antibacterial activity, as exhibited by the tail length (TL, 79.28 ± 4.54), olive tail moment (OTM, 40.4 ± 2.56), comet length (CL, 96.98 ± 9.28), and tail moment (TM, 51.75 ± 3.38). Therefore, a possible antibacterial mechanism was suggested as follows. i) Controlled NO release from MoS_2-BNN6 is achieved under 808 nm laser irradiation. ii) Simultaneously, the photothermal effect and

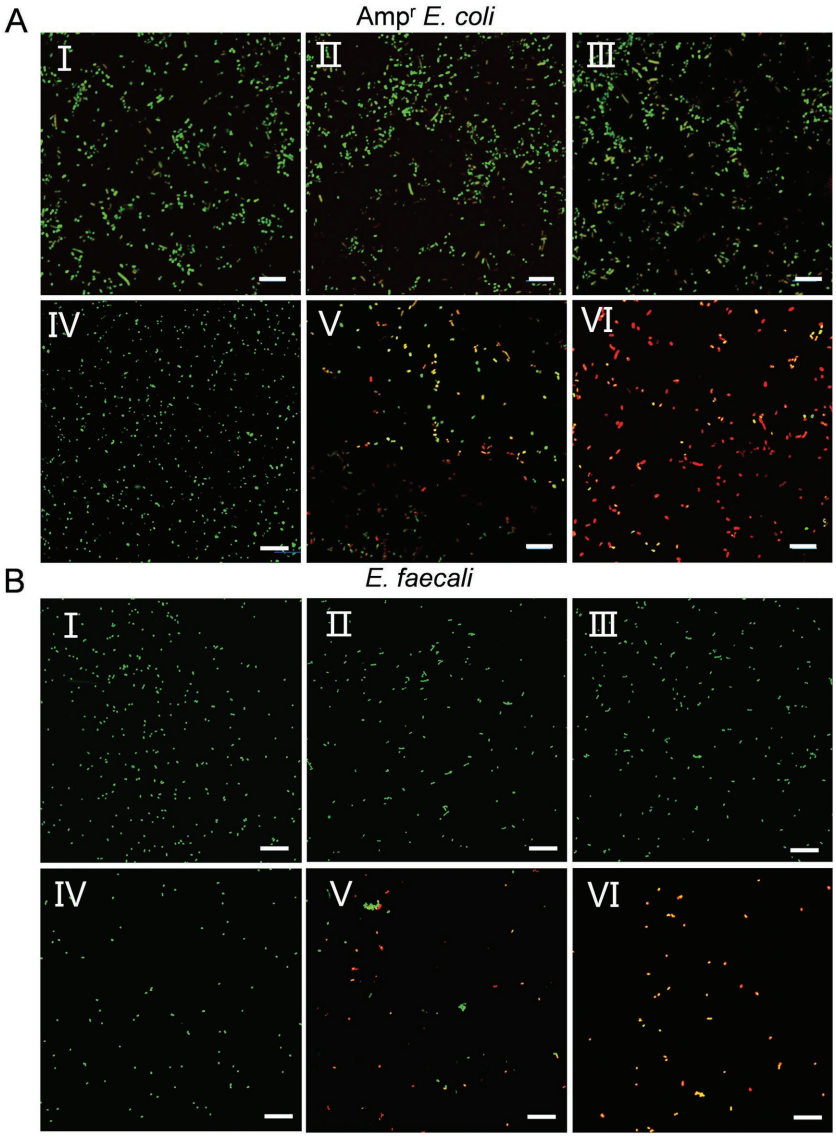

Figure 4. Fluorescence images of A) Amp^r *E. coli* and B) *E. faecalis* incubated with (I) PBS, (II) MoS_2-α-CD, (III) BNN6 + NIR, (IV) MoS_2-BNN6 + 50 °C, (V) MoS_2 + NIR, and (VI) MoS_2-BNN6 + NIR. Cells were costained with SYTO-9 and PI. Scale bars are 10 µm.

temperature-enhanced catalytic effect of MoS_2-BNN6 + NIR endow the nanovehicle with PTT/NO synergetic antibacterial activities to induce enhanced oxidative/nitrosative stress, even causing great DNA damage. In addition, it accelerates the oxidation of GSH, thereby reducing the removal of generated ROS/RNS in the bacteria and rapidly enhancing the biocidal effect.

To assess the biocompatibility of the nanovehicle, we performed viability assays on mammalian cells as well as a hemolysis assay on red blood cells (RBCs). The cytotoxicity of MoS_2-α-CD and MoS_2-BNN6 in human cervical carcinoma cells (HeLa), human umbilical vein endothelial cells lines (HUVEC), and human lung cancer cells (A549) was investigated by cell counting kit-8 (CCK-8) assay. After being treated with MoS_2-α-CD and MoS_2-BNN6 for 24 h, the viabilities of these cells were higher than 80%, even at nanosheet concentrations of up to 250 µg mL^{-1} (Figure S16A–C, Supporting Information). In addition, a hemolysis assay to investigate the impact of MoS_2-α-CD on RBCs, demonstrated that MoS_2-α-CD concentrations below 250 µg mL^{-1} showed negligible hemolysis of RBCs (Figure S16D, Supporting Information). These results indicate that both MoS_2-α-CD and MoS_2-BNN6 exhibited good biocompatibility.

To further demonstrate the practical applicability of this antibacterial strategy, we investigated its ability to promote wound healing in mice. **Figure 8** shows photographs and histological analyses of the healing of Amp^r *E. coli* infected wounds in mice that were subjected to different treatments. Compared with wounds before treatment (Figure S17, Supporting Information), a wound crust appeared at the MoS_2-BNN6 + NIR group dressed wound sites on the 6th day postsurgery (Figure 8A). Histological examinations using hematoxylin and eosin (H&E) staining were performed to evaluate the antibacterial activity of this strategy. The H&E staining in Figure 8B shows that the boundary between normal tissue and wound could be distinguished and scars began to appear in all groups on day 3. On day 6, the keratinocytes moved from the normal tissue to the wound site in all treatment groups, indicating the presence of apparent epithelial tissue. Surprisingly, the scars became markedly smaller and even disappeared after treatment with MoS_2-BNN6 + NIR, while there were incomplete dermal layers as well as wound boundaries in the other groups. Furthermore, Figure 8B shows the histological features based on Masson's Trichrome staining of collagen fibers for all groups. At day 6, although the wounds of the MoS_2-α-CD + NIR-treated group showed regeneration of collagen fibers, the MoS_2-BNN6 + NIR group demonstrated a much more significant increase in collagen fibers in the arbitrary collagen staining intensity and regeneration of the dermal layer. In Figure 8C, in comparison with other groups, the wound sizes of the MoS_2-BNN6 + NIR group clearly decreased. Furthermore, following these treatments, serum biochemical analysis (**Figure 9** and Figure S18, Supporting Information) and routine blood (Figure S19, Supporting Information) of the mice were performed to evaluate the antibacterial effect. A significant increase in lymphocytes (LY) and a decrease in granulocyte (GR) and monocyte percentages (MO%) for the control group with new Amp^r *E. coli*-infected wound were exhibited (Figure 9). However, in Figures S18 and S19 in the Supporting Information, all of the blood parameters were within the normal ranges when mice were treated with the synergetic treatment compared with the control group without wounds, implying an

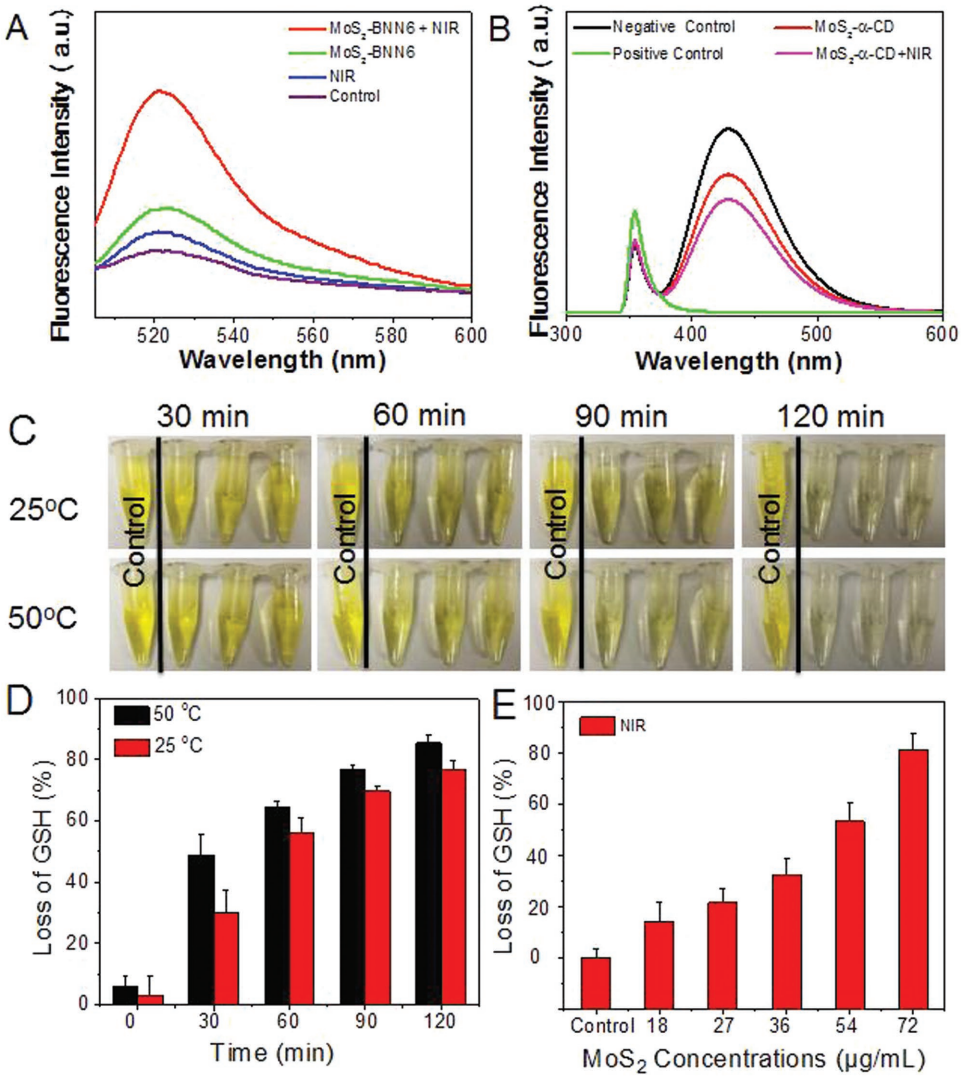

Figure 5. A) Measurement of ROS production in Amp^r *E. coli* using DCFH-DA assay when MoS_2-BNN6 exposed to 808 nm laser. B) Change of fluorescence intensities of OPA probe treated with Amp^r *E. coli* and MoS_2-α-CD without/with 808 nm laser in Tris–HCl buffer. C) Visual observation of color change after GSH treatment of MoS_2 with different time using water bath at 25 and 50 °C, respectively, determined by the Ellman's assay. D) Graph of lost GSH after incubation with MoS_2-α-CD at different time intervals corresponding to (C) under water bath at 25 and 50 °C, respectively. E) Graph of lost GSH after incubation with different concentrations of MoS_2-α-CD irradiated by 808 nm laser (1.0 W cm^{-2}).

enhanced antibacterial efficacy of the MoS_2-BNN6 + NIR group to wound healing through the elimination of inflammation. The increased body weight of the mice further indicated that the above synergetic therapy strategy is safe (Figure 8D). All of these results suggest that the synergistic antibacterial strategy can safely and effectively promote wound healing.

3. Conclusion

In summary, we have constructed a novel, biocompatible, 808 nm laser-mediated NO-releasing MoS_2-BNN6 nanovehicle by simple assembly of MoS_2-α-CD nanosheets with the NO donor BNN6 for low-cost, rapid, and effective treatment of typical Gram-negative and Gram-positive bacteria. When exposed to 808 nm laser irradiation, hyperthermia from MoS_2-BNN6 can precisely control NO delivery and release, to breakdown cell membranes through the PTT/NO synergy induced ROS/RNS. In parallel, MoS_2 can accelerate the oxidation of GSH under 808 nm irradiation, disrupting the balance of antioxidants in the bacteria and shortening the treatment time. Interestingly, the temperature-enhanced catalytic effect of MoS_2-α-CD verified by Ellman's assay, XANES and XPS could be the primary reason for the accelerated depletion of GSH. A possible antibacterial mechanism based on PTT/NO-enhanced free radical generation while reducing the GSH concentration was proposed. As a result, MoS_2-BNN6 + NIR achieved highly effective bacterial inactivation (>97.2%) within 10 min. Furthermore, the wound healing experiments demonstrated that this synergetic antibacterial strategy could be conveniently employed in highly efficient infected-wound disinfection and promotion of reconstruction of damaged tissues.

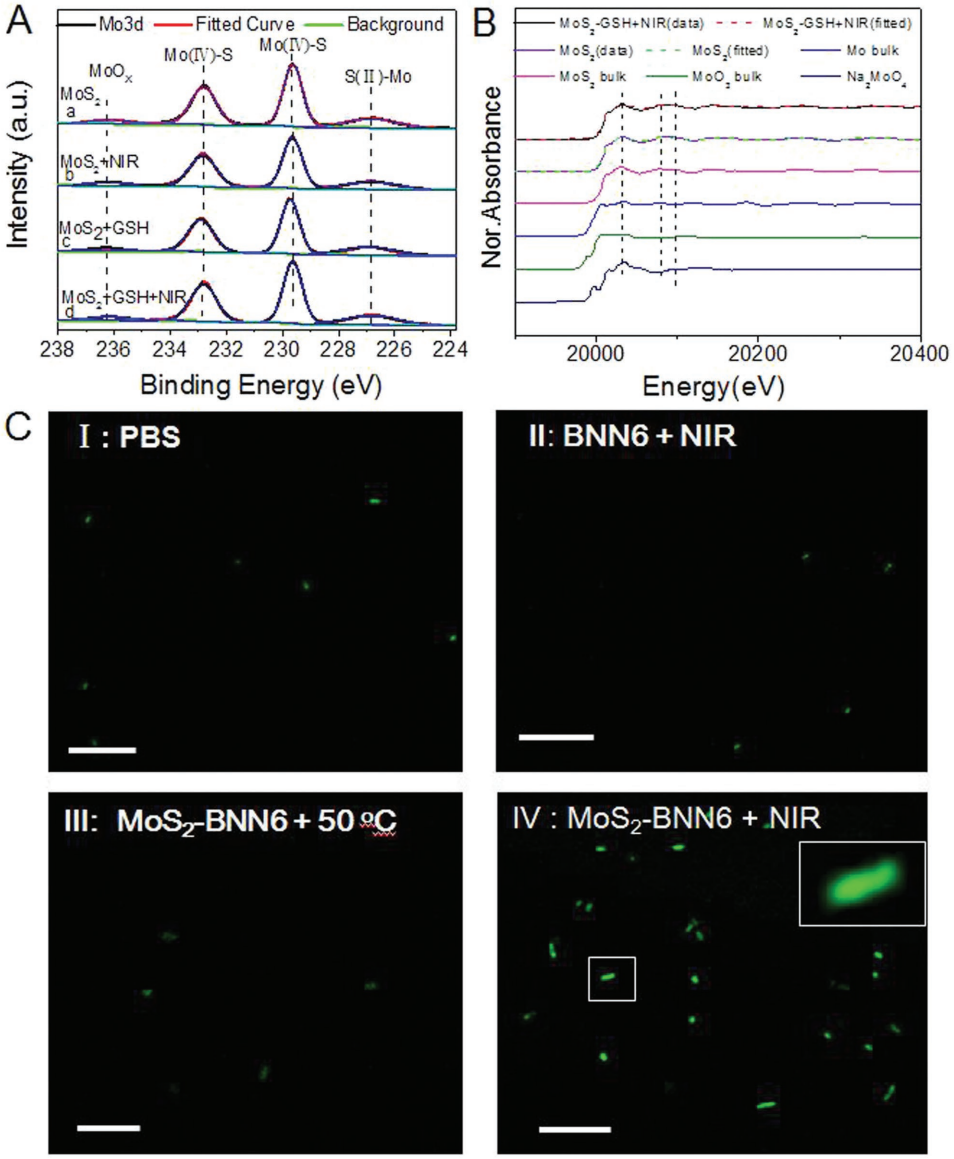

Figure 6. A) XPS spectra of Mo3d core-level for the MoS_2-α-CD and MoS_2-α-CD + GSH treated with/without NIR laser. B) Mo K-edge XANES spectra of MoS_2-α-CD and MoS_2-α-CD + GSH treated with/without 808 nm laser irradiation (1.0 W cm^{-2}, 10 min). C) Scanning confocal microscopy images of Amp^r *E. coli* incubated with DAF-FM DA after treated with (I) PBS, (II) BNN6 + NIR, (III) MoS_2-BNN6 + 50 °C, (IV) MoS_2-BNN6 + NIR. Inset in (IV) is magnified Amp^r *E. coli*. Scale bars are 20 µm.

4. Experimental Section

Materials: Molybdenum (IV) sulfide (MoS_2, 99%) was purchased from Alfa Aesar. α-cyclodextrin (α-CD) and *o*-phthaldialdehyde were provided by Aladdin Co., Ltd. *N*,*N*′-bis-sec-butylamino-*p*-phenylenediamine (BPA) was acquired from TCI America Inc. DAF-FM DA was supplied by Beyotime Biotechnology. Perchloric acid and sodium nitrite ($NaNO_2$) were provided by Sigma-Aldrich. Ethylenediaminetetraacetic acid (EDTA) was acquired from Aladdin Co., Ltd. Ethanol (C_2H_5OH), hydrochloric acid (HCl), and sodium hydroxide (NaOH) were obtained from Beijing Chemical Corporation. Deionized (DI) water was obtained from an 18 MΩ (SHRO-plus DI) system.

Characterization: The morphology of the products was characterized using a FE-SEM (S-4800, Hitachi, Japan) and a TEM (Tecnai G2 20 S-TWIN). FT-IR data were obtained from an infrared microscope (iN10-IZ10, Thermo Fisher). The topologies of the MoS_2 and MoS_2-α-CD nanosheets were examined by AFM (Agilent 5500, Agilent, USA) in tapping mode under ambient conditions. The UV–vis–NIR spectra were acquired using a U-3900 spectrophotometer (Hitachi). Dynamic light scatting was measured using a Nicomp380 ZLS plus ZETADi. The micro-Raman spectroscopy experiments were carried out under ambient conditions with 514 nm excitation from an argon ion laser (Renishawin Via Raman spectroscope). The TGA curve was obtained on a Diamond TG/DTA (Perkin Elmer). XPS measurements were carried out using an ESACLab220i-XL spectrometer with a twin-anode Al K_a (1486.6 eV) X-ray source.

Synthesis of α-CD Functionalized MoS_2 Nanosheets: MoS_2 nanosheets were synthesized using a modified liquid-phase exfoliation method based on our previous work.[58] In brief, commercial MoS_2 flakes (≈50 mg) were ground with a grinding machine for 10 h. The ground MoS_2 flakes were then dispersed in 50 mL of H_2SO_4 and heated to 90 °C for 24 h in an oil bath. The as-prepared products were collected by centrifugation

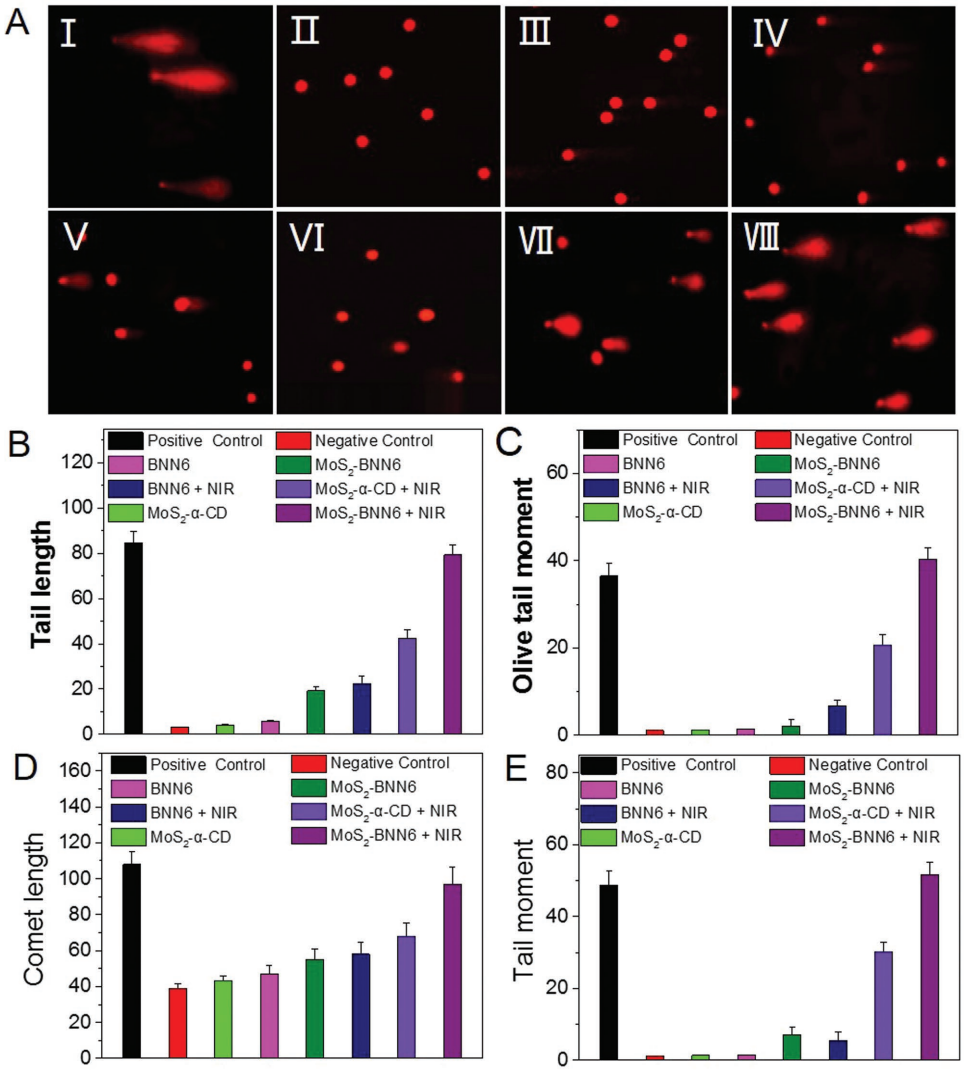

Figure 7. A) Comet assays for direct observation of DNA damages of Amp^r*E. coli* subjected to the following different treatments: (I) Positive control, (II) Negative control, (III) MoS_2-α-CD, (IV) BNN6, (V) MoS_2-BNN6, (VI) BNN6 + NIR, (VII) MoS_2 + NIR, and (VIII) MoS_2-BNN6 + NIR. B–E) Comparisons of comet assay parameters with different treatments (B: Tail length, C: Olive tail moment, D: Comet length, E: Tail moment) (power density: 1.0 W cm^{-2}, irradiation time: 10 min).

(5000 rpm, 5 min) and washed several times with deionized water. The H_2SO_4-treated MoS_2 dispersed in 45 mL of deionized water was then fragmented using a probe ultrasound homogenizer for 3 h. The aqueous suspension was centrifuged, and the resulting pellet was washed to give single-layer MoS_2 nanosheets.

To prepare the MoS_2-α-CD nanosheets, 40 mg of the as-prepared MoS_2 nanosheets were stirred in 10 mL of deionized water containing 200 mg of α-CD for 12 h at room temperature. The suspension was washed with deionized water three times to remove excess α-CD.

Synthesis of BNN6: *N*,*N*′-di-sec-butyl-*N*,*N*′-dinitroso-1,4-phenylenediamine (BNN6) was prepared according to a previously reported method.[59] Typically, 6.0 M of sodium nitrite (20 mL) was added to 18 mL of 4.27×10^{-3} M of BPA ethanol solution, while the mixed solution was stirred at room temperature under nitrogen for 30 min. Then, 20 mL of 6.0 M HCl was added dropwise to the reaction mixture and the color changed from red to orange. At the same time, a beige precipitate was produced. After 4 h, the products were washed several times with deionized water and 50% (v/v) ethanol/water to remove excess reagents. The product was dried and stored at −20 °C in the dark.

NIR Photothermal Effect: To investigate the photothermal effect of MoS_2-α-CD nanosheets, aqueous suspensions of MoS_2-α-CD with different concentrations (0, 3, 6, 12, 25, 50, 100, and 200 μg mL^{-1}) were added to a quartz cuvette. Water was used as a blank control. Afterward, the samples were irradiated with an 808 nm NIR laser (1.0 W cm^{-2}) for 600 s. The temperature was recorded every 15 s using a thermal imaging camera (E40, FLIR Corp., USA).

BNN6 Loading and NO Release: For the BNN6-loading experiment, 3 mg of MoS_2-α-CD nanosheets were mixed with 3 mL of BNN6 solutions with different concentrations (0, 50, 100, 300, 500, and 800 μg mL^{-1} in water containing ≈33% ethanol) and stirred in brown vials for 24 h at 25 °C. Subsequently, the BNN6-loaded MoS_2-α-CD (MoS_2-BNN6) were centrifuged and washed with deionized water. The loading capacity was measured using UV–vis absorption of BNN6 at 265 nm. The BNN6 loading efficiency was determined by the following equation

$$\text{Loading efficiency}\,(\%) = \frac{(C_0 - C_e) \times V}{m} \times 100\% \quad (1)$$

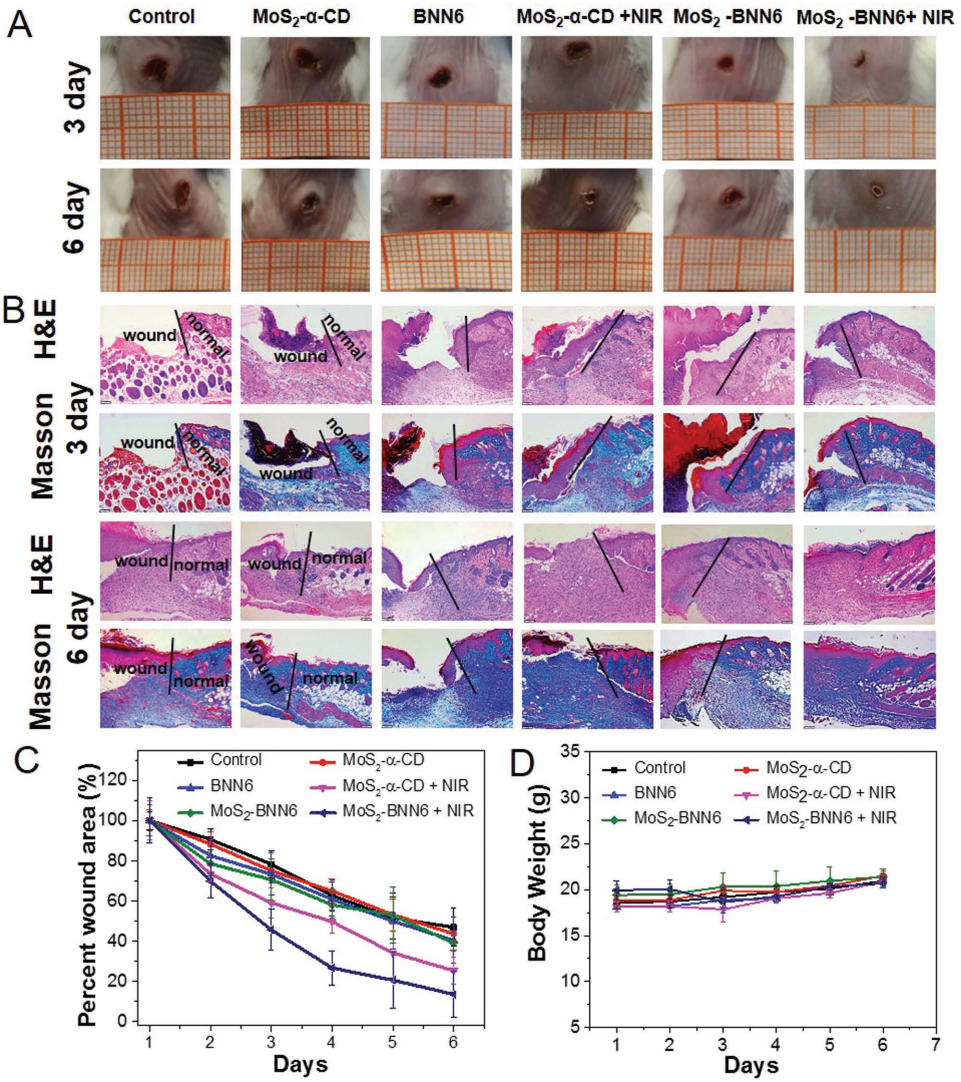

Figure 8. In vivo antibacterial efficacy of PTT/NO synergetic strategy. A) Visual observation of healing process upon Amp^r *E. coli* infected wounds treated with control (PBS), MoS_2-α-CD, BNN6, MoS_2-α-CD + NIR, MoS_2-BNN6, and MoS_2-BNN6 + NIR. B) Histologic analyses of Amp^r *E. coli*-infected wounds treated with PBS, MoS_2-α-CD, BNN6, MoS_2-α-CD + NIR, MoS_2-BNN6, and MoS_2-BNN6 + NIR at the 3rd and 6th day. C) Graphical representation of quantitative measurement of wound area within 6 d. D) Changes in mice body weight during the treatment.

where V (mL) is the volume of the final supernatant, C_0 (μg mL^{-1}) and C_e (μg mL^{-1}) are the initial and equilibrium concentrations of BNN6 aqueous solution, respectively, and m (mg) is the mass of MoS_2-α-CD.

Exposure of the MoS_2-BNN6 nanovehicle to 808 nm laser irradiation led to the decomposition of BNN6 into NO and BHA, illustrated in Figure S7 in the Supporting Information, wherein BHA represents the byproduct of the decomposition of BNN6. For quantitative detection of the controlled NO release from MoS_2-BNN6, a saturated adsorption solution of MoS_2-BNN6 (200 μg mL^{-1} based on the concentration of MoS_2-α-CD, with equivalent BNN6 of 80 μg mL^{-1}) was added to a tube and stirred in the dark while being irradiated with an 808 nm NIR laser for a certain time with different power densities (0.3, 0.6, and 1.0 W cm^{-2}). After centrifugation, the NO released from the supernatants of BNN6 and MoS_2-BNN6 was quantified using a commercial fluorescent probe DAN.

In brief, 1 mg of DAN was dissolved into 20 mL of HCl (0.62 M), then 10 μL of DAN solution was mixed with 100 μL of the above supernatant, and the mixture was incubated in the dark for 10 min at room temperature. Then, 5 μL of NaOH (2.8 M) added, and the mixture was diluted with 4 mL of deionized water for fluorescence spectroscopy measurement (Horiba Jobin Yvon FluoroLog3). The standard curve was established with commercial $NaNO_2$ as a standard (0–10 × 10^{-6} M) before quantification of the released NO concentration. Excitation wavelength: 365 nm, emission wavelength: 405 nm.

Additionally, NO was also detected and quantified using a Free Radical Analyzer with a NO electrode (TBR 1025 and ISO-NOP, World Precision Instruments). Before measurement, the standard curve should be established by chemical generation of NO using 0.1 M H_2SO_4, 0.1 M KI and 50 × 10^{-6} M KNO_2. After that, MoS_2-BNN6 were dispersed in PBS solution (100 μg mL^{-1}), and then irradiated under 808 nm laser. The amount of NO was calculated from the recorded current and standard curve.

Bacterial Culture: To obtain bacterial solutions, a monocolony of Gram-positive *Escherichia faecalis* (*E. faecalis*) cultured on a solid tryptone soy (TS) agar plate was transferred to 15 mL of TS broth and shaken at 200 rpm for 6 h at 37 °C. The bacterial solution was then centrifuged and washed with sterile PBS (8000 rpm for 1 min). The precipitated bacteria were suspended and diluted to an optical density

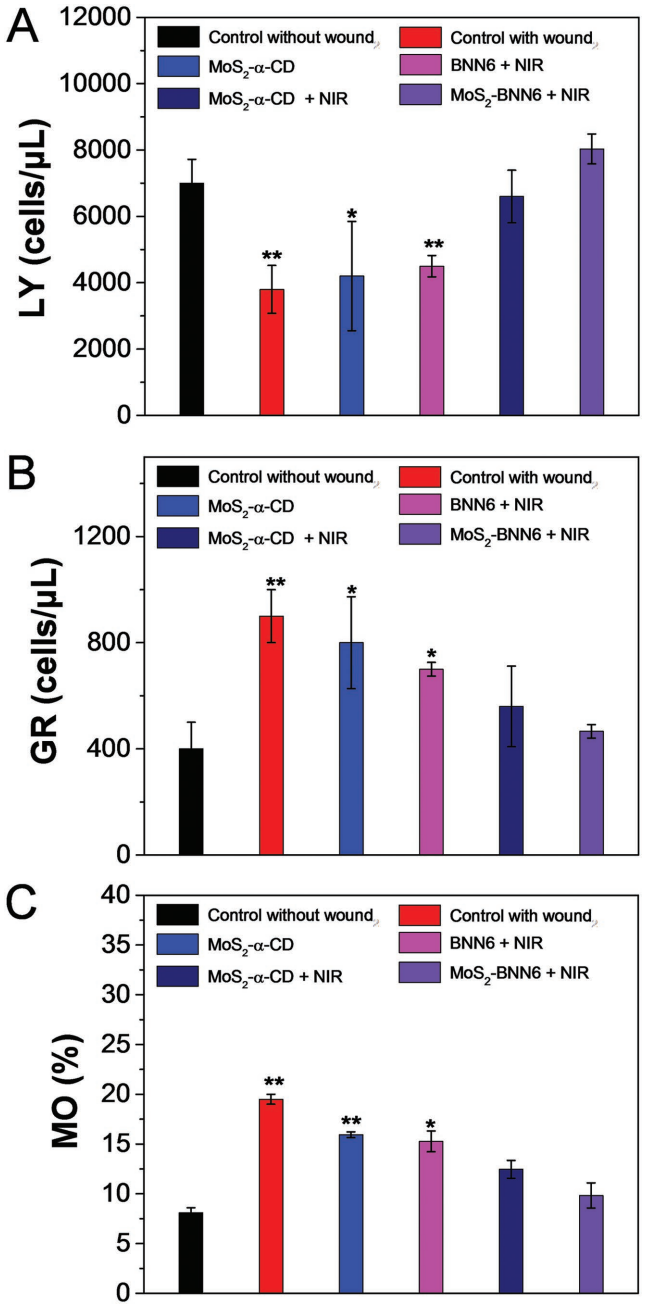

Figure 9. Comparative analyses of hematological traits A) lymphocytes (LY), B) granulocytes (GR), and C) monocytes percentage (MO%) of mice suffering from infected wound treatments with control (with fresh wound, without wound), MoS_2-α-CD, BNN6 + NIR, MoS_2-α-CD + NIR, and MoS_2-BNN6 + NIR on day 6.

of 0.1 at 600 nm (OD_{600} = 0.1, with equivalent 1.0×10^8 CFU mL^{-1}) with PBS for antibacterial evaluation. Gram-negative ampicillin-resistant *Escherichia coli* (Amp^r *E. coli*) were then grown on Luria–Bertani (LB) agar plates, and 50 μg mL^{-1} of ampicillin was added to the LB culture media. The culture method for Amp^r *E. coli* was similar to the culture process for *E. faecalis*.

NIR Laser-Mediated PTT/NO Synergetic Antibacterial Effects In Vitro: Before investigating the NIR laser-mediated synergetic photothermal/NO antibacterial effects, the OD_{600} (optical density at 600 nm) method was used to evaluate the antibacterial capacities of BNN6, MoS_2-α-CD, and MoS_2-BNN6 against bacteria. Amp^r *E. coli* (1.0×10^5 CFU mL^{-1}) were incubated separately with different concentrations of BNN6 (0, 2.5, 5, 10, 20, 40, and 80 μg mL^{-1}), MoS_2-α-CD (0, 6.25, 12.5, 25, 50, 100, and 200 μg mL^{-1}), and MoS_2-BNN6 (0, 6.25, 12.5, 25, 50, 100, and 200 μg mL^{-1}, based on MoS_2-α-CD concentrations) dispersed in LB culture at 180 rpm (16 h, 37 °C). The absorbance at 600 nm was then measured. LB medium without bacteria was used as a blank experimental group. Untreated bacteria solution was used as a control experimental group.

The antibacterial properties of the synergetic PTT/NO were measured using a plate counting method. For this, 400 μL of 10^4 CFU mL^{-1} bacterial solutions (Amp^r *E. coli* or *E. faecalis*) and 100 μL of different concentrations of MoS_2-α-CD, BNN6, or MoS_2-BNN6 were added to 48-well microtiter plates. The final concentrations of MoS_2-α-CD, BNN6, or MoS_2-BNN6 (based on the concentration of MoS_2-α-CD) were 200, 80, and 200 μg mL^{-1}, respectively. The above mixtures were irradiated with an 808 nm laser (1.0 W cm^{-2}) or left untreated for 10 min. Then, 100 μL of the collected bacterial suspension was transferred to a solid medium and incubated for 16 h at 37 °C to observe the morphology of the clones. Colonies were calculated and compared with those on the control plates to evaluate the relative activities of the bacteria. The control experimental group was untreated bacteria. All experimental groups were measured in triplicate.

In addition, Gram-positive *Staphylococcus aureus* (*S. aureus*) always occurs on the body surface of mammals. Therefore, *S. aureus* was selected to testify the antibacterial property of the synergetic PTT/NO system using plate counting method. Typically, *S. aureus* solutions were cultivated in a liquid LB medium at 37 °C at 220 rpm in a rotary shaker for 16 h. Before the experiment, the *S. aureus* solutions were diluted to 10^5 CFU mL^{-1} and MoS_2-α-CD, BNN6, or MoS_2-BNN6 with final concentrations of 200, 80, and 200 μg mL^{-1} were respectively added to the *S. aureus* solutions. Then, the above mixtures were irradiated with 808 nm laser or left untreated for 10 min. Finally, 50 μL of the collected bacterial suspension in each treatment was transferred to solid medium and incubated for 16 h at 37 °C. The morphologies of the clones were observed and the number of clones was counted. The control experimental group was untreated bacteria. All experimental groups were measured in triplicate.

FE-SEM images were acquired to show the damage to the bacteria caused by MoS_2-BNN6 + NIR. First, Amp^r *E. coli* and *E. faecalis* treated with the different materials were divided into eight groups including PBS, MoS_2-α-CD, BNN6, MoS_2-BNN6, PBS + NIR, MoS_2-α-CD + NIR, BNN6 + NIR, and MoS_2-BNN6 + NIR. The bacteria solutions were fixed with 4% paraformaldehyde at 4 °C for 4 h and then dropped onto silicon. The bacteria were dehydrated with ethanol sequentially over 10 min. The volume percentages of ethanol in water were 30%, 50%, 70%, 80%, 90%, and 100%.

Live/Dead Bacterial Cell Staining: SYTO-9 and PI were used to distinguish between live and dead microbial cells. SYTO-9 labels bacterial cells in green owing to penetrating all bacterial membranes (intact and damaged), while PI can only penetrate injured cell membranes labeling the cells red while diminishing the green resulting from SYTO-9 staining.[43] In detail, 400 μL of Amp^r *E. coli* or *E. faecalsi* (10^8 CFU mL^{-1}) culture suspensions treated with MoS_2, BNN6 + NIR, MoS_2-BNN6 + 50 °C, MoS_2 + NIR, or MoS_2-BNN6 + NIR, were treated with 20 μL of SYTO-9 (1.0×10^{-3} M) and 20 μL of PI (1.5×10^{-3} M) in the dark for 15 min at 37 °C. After staining, the treated samples were centrifuged with PBS to remove excess SYTO-9 and PI. Bacteria were then resuspended in 50 μL of PBS and placed on the surfaces of slides. The slides were used to capture the images of the stained Amp^r *E. coli* or *E. faecalis* using confocal fluorescence microscopy using a 60× magnification.

Detection of the Intracellular GSH Level: It is well known that the disproportionation reaction of adjacent aldehyde groups in *o*-phthalaldehyde (OPA) leads to a derivatization reaction with GSH to produce two isoindole derivatives of tricyclic and bicyclic structures in Tris–HCl buffer, and the tricyclic structure has strong fluorescence.[60,61] Therefore, the intracellular GSH level was measured using an OPA fluorescent probe. First, Amp^r *E. coli* (10^8 CFU mL^{-1}) were treated with 50 μg mL^{-1} of MoS_2 or MoS_2-BNN6 for 4 h with or without 808 nm

laser irradiation. Cells were then lysed with 100 µL of 1% perchloric acid for 15 min on ice. Then, 100 µL of the cell lysate was mixed with Tris–HCl (900 µL, pH = 8.3 × 10^{-3}, 50 × 10^{-3} M) containing 100 µL of OPA (1 mg mL^{-1}) and incubated for 90 min at 150 rpm in the dark at 30 °C. The MoS_2 or MoS_2-BNN6 lysate solutions were removed by centrifugation at a speed of 12 000 rpm. The fluorescence intensity was measured using a spectrofluorometer. Excitation wavelength: 350 nm, emission wavelength: 420 nm. Untreated bacteria and H_2O_2 (1.0 × 10^{-3} M)-treated bacteria were regarded as negative and positive control groups, respectively.

Detection of Intracellular ROS: In this procedure, 2′,7′-dichlorofluorescin diacetate (DCFH-DA, Beyotime Biotechnology Company) was used to detect the oxidative species in *E.coli*. After reacting with oxidizing species, DCFH-DA is oxidized to fluorescent 2′,7′-dichlorofluorescin (DCFH). In brief, *E. coli* (10^8 CFU mL^{-1}) was incubated with 20 × 10^{-6} M of DCFH-DA at 37 °C for 30 min in the dark. The cells were then treated with MoS_2-α-CD, BNN6 + NIR, MoS_2-BNN6, MoS_2-α-CD + NIR, or MoS_2-BNN6 + NIR (power density: 1.0 W cm^{-2}, time: 10 min). The fluorescence spectra of the bacterial suspensions were recorded on a Horiba Jobin Yvon FluoroLog3 spectrofluorometer at an excitation wavelength of 488 nm.

Evaluation of GSH Oxidation: The changes in GSH concentration were assessed using were assessed using Ellman's experiments.[33] Typically, 225 µL of MoS_2-α-CD nanosheets (150 µg mL^{-1}) dispersed in bicarbonate buffer solution (50 × 10^{-3} M, pH = 8.7) were mixed well with 1.0 × 10^{-3} M GSH bicarbonate buffer solution (225 µL) and incubated for 30, 60, 90, and 120 min with mixing at 180 rpm at 25 and 50 °C in the dark. 785 µL of 0.05 M Tris-HCl (pH = 8) solution and 15 µL of 100 × 10^{-3} M 5,5′-dithiobis (2-nitrobenzoic acid) (Ellman's reagent) were mixed with bicarbonate buffer solution to yield a yellow product. To remove the effect of MoS_2, the MoS_2-α-CD nanosheets in the as-obtained solutions were removed by centrifugation at 12 000 rpm. 200 µL of the supernatant was then collected in 96-well plates. The loss of GSH was evaluated by measuring the absorbance at 410 nm with a microplate spectrophotometer (Multiskan MK3, Thermo Scientific). 1 × 10^{-3} M of GSH solution was used as a negative control group.

An Ellman experiment was also used to explore the GSH oxidation induced by different concentrations (18, 27, 36, 54, and 72 µg mL^{-1}) of MoS_2-α-CD with irradiation at 808 nm.

XANES Characterization: To elucidate the mechanism of the GSH oxidation induced by MoS_2-α-CD with 808 nm laser irradiation, the XANES spectra of the Mo K-edge in MoS_2-α-CD and MoS_2-α-CD + GSH with and without 808 nm irradiation were measured. First, the as-tested dispersions were irradiated with 808 nm laser for 10 min and the temperature was maintained at 50 °C. Reference samples including Mo, MoS_2, MoO_3, and Na_2MoO_4 were used to fit the XANES results of the tested dispersions. The XANES spectra were acquired on beamline 1W1B at the Beijing Synchrotron Radiation Facility. The ring storage energy of the synchrotron radiation accelerator during data collection was 2.5 GeV with a current intensity of 50 mA. Mo K-edge XANES spectra of the reference samples for Mo were measured using transmission mode. Fluorescence mode was applied for acquisition of the Mo K-edge spectra of experimental samples using a 19-element germanium array solid detector. The XANES spectra data was normalized and linearly fitted by Athena software.

Intracellular NO Measurement: A commercial NO fluorescent probe DAF-FM DA was used to detect the release of NO from MoS_2-BNN6 in bacteria. DAF-FM DA does not react with NO itself but with its byproducts such as nitric anhydride (N_2O_3), peroxynitrite ($ONOO^-$), which are formed by autoxidation of NO.[50] Typically, OD_{600} = 0.1 of Amp^r *E. coli* suspended in PBS containing DAF-FM DA (10 × 10^{-3} M) was incubated at 37 °C for 30 min then washed three times with PBS. After loading the fluorescent probe, MoS_2-α-CD or MoS_2-BNN6 was added to the Amp^r *E. coli* suspensions and the mixture was irradiated with an 808 nm laser or heated directly using a water bath for 10 min. 20 µL of the bacterial solution loaded with DAF-FM DA was transferred onto slides to acquire Amp^r *E. coli* images using confocal fluorescence microscopy (ALR-Si, Nikon, shanghai). Excitation wavelength: 495 nm; emission wavelength: 515 nm.

Comet Assay: DNA damage was evaluated by single cell gel electrophoresis (comet assay).[52] Briefly, 400 µL of 2 × 10^6 CFU mL^{-1} Amp^r *E. coli* and 100 µL of MoS_2-α-CD (200 µg mL^{-1}), BNN6 (80 µg mL^{-1}), and MoS_2-BNN6 (200 µg mL^{-1}) were added to 48-well microtiter plates. All experimental groups were tested in triplicate. 100 µL of H_2O_2 (100 × 10^{-6} M) was added to 400 µL of bacteria solution as a positive control. For the 808 nm laser irradiation groups, the above mixture was treated for 10 min with an 808 nm laser (1.0 W cm^{-2}). 20 µL of bacteria solution was then added to 80 µL of 0.5% low melting point agarose at 37 °C and immediately scribbled on the surface of the slides which were precoated with 1% normal melting point agarose. When the gel had solidified, the slides were immersed in lysis solution (GMS10082.1 v.A) at 4 °C for 2 h in the dark. The slides were then denatured in alkaline buffer (1.0 × 10^{-3} M EDTA and 300 × 10^{-3} M NaOH) for 20 min, followed by electrophoresis at 25 V, 300 mA for 20 min. The samples were neutralized in 0.5 M Tris-HCl (pH = 6.8) for 10 min and incubated with 35 µL of staining solution (GMS10082.1 v. A) for 10 min. The slides were used to identify DNA damage under confocal fluorescence microscopy (ALR-Si, Nikon, Shanghai) using 40 × magnification. A total of ten images per sample were acquired for analysis and the free version of a manual scoring program Comet Score was used to calculate four parameters: CL, TL, TM, and OTM.

Cytotoxicity Assay and Hemolysis Analysis In Vitro: Human cervical carcinoma cells (HeLa), HUVEC, and human lung cancer cells (A549) were obtained from the Cancer Hospital Chinese Academy of Medical Sciences. The three cell lines were selected to explore the cell viabilities using a standard CCK-8. The cells were cultured in normal Dulbecco's modified eagle medium (DMEM) culture medium containing 10% fetal bovine serum in a 96-well culture plate at a density of 8000 cells $well^{-1}$ and kept in an atmosphere of 5% CO_2 at 37 °C for 24 h. Subsequently, the cells were incubated with MoS_2-α-CD of different concentrations (0, 3.91, 7.81, 15.63, 31.25, 62.5, 125, and 250 µg mL^{-1}) for a further 24 h. The cells were then washed with PBS (0.01 M, pH = 7.4) twice and recultured with DMEM containing CCK-8 (10%) for 1.5 h. Cell viabilities were determined from the characteristic peak at 450 nm using a microplate reader (SpectraMax M2, MDC, USA).

For the in vitro hemolysis analysis, a sample of 1 mL of blood obtained from a 6-week-old BALB/c mouse was mixed with 3 mL of PBS containing EDTA. RBCs were separated from the blood by centrifugation at 2000 rpm. The RBCs were then washed three times with PBS and resuspended in PBS. Subsequently, 0.2 mL of diluted RBC suspension was added to 0.8 mL of PBS (negative control), 0.8 mL of deionized water (positive control), and 0.8 mL of MoS_2-α-CD dispersion at concentrations ranging from 3.9 to 250 µg mL^{-1}. Finally, the samples were kept at room temperature for 4 h and centrifuged at 12 000 rpm. The absorbance of the supernatants at 541 nm was measured by UV–vis spectrophotometry.

Wound Healing and Inflammation Assay In Vivo: All animal experiments were approved by the local animal ethics committee of the National Center for Nanoscience and Technology, Chinese Academy of Science. Typically, six weeks-old female BALB/c mice were used (n = 8 for each group) and divided into PBS, MoS_2-α-CD, BNN6, MoS_2-α-CD + NIR, MoS_2-BNN6, and MoS_2-BNN6 + NIR groups. The back hair of each mouse was shaved off before a wound of d = 5 mm was administered by surgical procedure. The skin wounds were preprocessed with Amp^r *E. coli* suspensions (1 × 10^4 CFU mL^{-1}) for 24 h. After 1 d, the infected wound areas were treated with the following solutions MoS_2-α-CD (200 µg mL^{-1}), BNN6 (80 µg mL^{-1}), and MoS_2-BNN6 (200 µg mL^{-1} based on MoS_2-α-CD concentration) in the corresponding groups. In the 808 nm laser treated groups, the wounds were treated for 10 min at a power density of 0.5 W cm^{-2}. Subsequently, the wounds were digitally photographed using a COOLPIX P900S camera on days 1, 3, and 6. Changes in wound sizes were measured using an image analysis program (Image J, National Institutes of Health). Three mice per group were euthanized on days 3 and 6. For histological analysis of hematoxylin and eosin (H&E) staining and Masson's trichrome staining, the skin of the wounds was excised and fixed with 10% formalin. On day 6, blood samples were obtained from the fundus artery of the mice. 1 mL of blood

was centrifuged at 2500 rpm for 15 min after sitting at room temperature for 2 h. The collected serum was then used in biochemical testing. The following five parameters were evaluated: alanine aminotransferase, aspartate aminotransferase, urea, creatinine, and creatine kinase. Routine blood analysis was carried out on 200 µL of each blood sample, which was mixed with an anticoagulant, EDTA. Routine blood analysis included GR, LY, MO%, RBCs, red blood cell volume distribution width, hemoglobin, mean corpuscular hemoglobin, mean corpuscular hemoglobin concentration, hematocrit, mean corpuscular volume, mean platelet volume, and platelet distribution width.

Statistical Analysis: All the experiments were performed in triplicate. The obtained data were expressed as the mean value ± standard deviation, and the statistical significance between two groups was analyzed by the Student's *t*-test. Single and double asterisks $*p < 0.05$ was considered statistically significant and $**p < 0.01$ were extremely significant.

Supporting Information

Supporting Information is available from the Willey Online Library or from the author.

Acknowledgements

Q.G. and X.Z. contributed equally to this work. This work was supported by the National Basic Research Programs of China (2016YFA0201600 and 2015CB932104), Beijing Natural Science Foundation (2162046), and National Natural Science Foundation of China (51772293, 51772292, 11621505, 31571015, and 21320102003), and Military Medical Science and Technology Innovation Program of Southwest Hospital (SWH2016LHJC-07, SWH2016JCYB-01, and SWH2017YQPY-03).

Conflict of Interest

The authors declare no conflict of interest.

Keywords

hyperthermia, light-mediated synergetic therapy, MoS_2, wound disinfection and healing

Received: June 14, 2018
Revised: August 17, 2018
Published online:

[1] A. L. Hook, C. Y. Chang, J. Yang, S. Atkinson, R. Langer, D. G. Anderson, M. C. Davies, P. Williams, M. R. Alexander, *Adv. Mater.* **2013**, *25*, 2542.
[2] Z. Wang, K. Dong, Z. Liu, Y. Zhang, Z. Chen, H. Sun, J. Ren, X. Qu, *Biomaterials* **2017**, *113*, 145.
[3] R. J. Fair, Y. Tor, *Perspect. Med. Chem.* **2014**, *6*, PMC.S14459.
[4] H. J. Jian, R. S. Wu, T. Y. Lin, Y. J. Li, H. J. Lin, S. G. Harroun, J. Y. Lai, C. C. Huang, *ACS Nano* **2017**, *11*, 6703.
[5] C. Zhu, Q. Yang, L. Liu, F. Lv, S. Li, G. Yang, S. Wang, *Adv. Mater.* **2011**, *23*, 4805.
[6] B. Z. Ristic, M. M. Milenkovic, I. R. Dakic, B. M. Todorovic-Markovic, M. S. Milosavljevic, M. D. Budimir, V. G. Paunovic, M. D. Dramicanin, Z. M. Markovic, V. S. Trajkovic, *Biomaterials* **2014**, *35*, 4428.
[7] D. Hu, H. Li, B. Wang, Z. Ye, W. Lei, F. Jia, Q. Jin, K. F. Ren, J. Ji, *ACS Nano* **2017**, *11*, 9330.
[8] S. Pandit, S. Karunakaran, S. K. Boda, B. Basu, M. De, *ACS Appl. Mater. Interfaces* **2016**, *8*, 31567.
[9] A. Fakhri, P. A. Nejad, *J. Photochem. Photobiol., B* **2016**, *159*, 211.
[10] H. Zheng, R. Ma, M. Gao, X. Tian, Y. Q. Li, L. Zeng, R. Li, *Sci. Bull.* **2017**, *7*, 133.
[11] Y. Li, X. Liu, L. Tan, Z. Cui, X. Yang, Y. Zheng, K. W. K. Yeung, P. K. Chu, S. Wu, *Adv. Funct. Mater.* **2018**, *28*, 1800299.
[12] C. Mao, Y. Xiang, X. Liu, Z. Cui, X. Yang, K. W. K. Yeung, H. Pan, X. Wang, P. K. Chu, S. Wu, *ACS Nano* **2017**, *11*, 9010.
[13] C. Mao, Y. Xiang, X. Liu, Z. Cui, X. Yang, Z. Li, S. Zhu, Y. Zheng, W. K. W. Yeung, S. Wu, *ACS Nano* **2018**, *12*, 1747.
[14] M. Yin, Z. Li, E. Ju, Z. Wang, K. Dong, J. Ren, X. Qu, *Chem. Commun.* **2014**, *50*, 10488.
[15] W. Yin, J. Yu, F. Lv, L. Yan, L. R. Zheng, Z. Gu, Y. Zhao, *ACS Nano* **2016**, *10*, 11000.
[16] L. Tan, J. Li, X. Liu, Z. Cui, X. Yang, S. Zhu, Z. Li, X. Yuan, Y. Zheng, K. W. K. Yeung, H. Pan, X. Wang, S. Wu, *Adv. Mater.* **2018**, *30*, 1801808.
[17] X. Yang, Z. Li, E. Ju, J. Ren, X. Qu, *Chem. - Eur. J.* **2014**, *20*, 394.
[18] M. S. Laport, M. R. da Silva, C. C. Silva, M. do Carmo de Freire Bastos, *Curr. Microbiol.* **2003**, *46*, 313.
[19] S. Municoy, M. F. Desimone, P. N. Catalano, M. G. Bellino, *Curr. Bionanotechnol. (Discontinued)* **2015**, *1*, 125.
[20] D. Huo, J. Gao, B. Guo, Y. Ding, J. He, H. Yu, Z. Zhou, Y. Hu, *RSC Adv.* **2013**, *3*, 10632.
[21] A. Ghaffari, C. Miller, B. McMullin, A. P. Ghahary, *Nitric Oxide* **2006**, *14*, 21.
[22] T. K. Nguyen, R. Selvanayagam, K. K. Ho, R. Chen, S. K. Kutty, S. A. Rice, N. Kumar, N. Barraud, H. T. Duong, C. Boyer, *Chem. Sci.* **2016**, *7*, 1016.
[23] M. T. Pelegrino, R. B. Weller, X. Chen, J. S. Bernardes, A. B. Seabra, *MedChemComm* **2017**, *8*, 713.
[24] E. M. Hetrick, J. H. Shin, N. A. Stasko, C. B. Johnson, D. A. Wespe, E. Holmuhamedov, M. H. Schoenfisch, *ACS Nano* **2008**, *2*, 235.
[25] P. G. Wang, M. Xian, X. Tang, X. Wu, Z. Wen, T. Cai, A. J. Janczuk, *Chem. Rev.* **2002**, *102*, 1091.
[26] J. A. Hrabie, L. K. Keefer, *Chem. Rev.* **2002**, *102*, 1135.
[27] S. P. Goss, N. Hogg, B. Kalyanaraman, *J. Biol. Chem.* **1997**, *272*, 21647.
[28] T. Yamamoto, R. J. Bing, *Proc. Soc. Exp. Biol. Med.* **2000**, *225*, 200.
[29] J. Gehring, B. Trepka, N. Klinkenberg, H. Bronner, D. Schleheck, S. Polarz, *J. Am. Chem. Soc.* **2016**, *138*, 3076.
[30] B. J. Privett, S. M. Deupree, C. J. Backlund, K. S. Rao, C. B. Johnson, P. N. Coneski, M. H. Schoenfisch, *Mol. Pharmaceutics* **2010**, *7*, 2289.
[31] T. Liu, Y. Chao, M. Gao, C. Liang, Q. Chen, G. Song, L. Cheng, Z. Liu, *Nano Res.* **2016**, *9*, 3003.
[32] S. S. Chou, B. Kaehr, J. Kim, B. M. Foley, M. De, P. E. Hopkins, J. Huang, C. J. Brinker, V. P. Dravid, *Angew. Chem., Int. Ed.* **2013**, *52*, 4160.
[33] S. C. Chen, C. Y. Lin, T. L. Cheng, W. L. Tseng, *Adv. Funct. Mater.* **2017**, *27*, 1702452.
[34] T. Liu, S. Shi, C. Liang, S. Shen, L. Cheng, C. Wang, X. Song, S. Goel, T. E. Barnhart, W. Cai, Z. Liu, *ACS Nano* **2015**, *9*, 950.
[35] W. Z. Teo, E. L. K. Chng, Z. Sofer, M. Pumera, *Chem. - Eur. J.* **2014**, *20*, 9627.
[36] J. Yu, W. Yin, X. Zheng, G. Tian, X. Zhang, T. Bao, X. Dong, Z. Wang, Z. Gu, X. Ma, Y. Zhao, *Theranostics* **2015**, *5*, 931.
[37] X. Yang, J. Li, T. Liang, C. Ma, Y. Zhang, H. Chen, N. Hanagata, H. Su, M. Xu, *Nanoscale* **2014**, *6*, 10126.
[38] Y. X. Wang, S. L. Chou, D. Wexler, H. K. Liu, S.-X. Dou, *Chem. - Eur. J.* **2014**, *20*, 9607.
[39] X. Zou, L. Zhang, Z. Wang, Y. Luo, *J. Am. Chem. Soc.* **2016**, *138*, 2064.

[40] X. Wei, J. Gao, F. Wang, M. Ying, P. Angsantikul, A. V. Kroll, J. Zhou, W. Gao, W. Lu, R. H. Fang, L. Zhang, *Adv. Mater.* **2017**, *29*, 1701644.
[41] T. Tsuchido, N. Katsui, A. Takeuchi, M. Takano, I. Shibasaki, *Appl. Environ. Microbiol.* **1985**, *50*, 298.
[42] W. Yin, X. Dong, J. Yu, J. Pan, Z. Yao, Z. Gu, Y. Zhao, *ACS Appl. Mater. Interfaces* **2017**, *9*, 21362.
[43] H. S. S. Ramakrishna Matte, A. Gomathi, A. K. Manna, D. J. Late, R. Datta, S. K. Pati, C. N. R. Rao, *Angew. Chem., Int. Ed.* **2010**, *49*, 4059.
[44] M. A. Lukowski, A. S. Daniel, F. Meng, A. Forticaux, L. Li, S. Jin, *J. Am. Chem. Soc.* **2013**, *135*, 10274.
[45] Z. Feng, X. Liu, L. Tan, Z. Cui, X. Yang, Z. Li, Y. Zheng, K. M. K. Yeung, S. Wu, *Small* **2018**, *14*, 1704347.
[46] X. Zhu, W. Feng, J. Chang, Y. W. Tan, J. Li, M. Chen, Y. Sun, F. Li, *Nat. Commun.* **2016**, *7*, 10437.
[47] S. George, A. Kishen, *Photochem. Photobiol.* **2008**, *84*, 734.
[48] M. Vukomanović, V. Zunic, S. Kunej, B. Jancar, S. Jeverica, D. Suvorov, *Sci. Rep.* **2017**, *7*, 4324.
[49] Y. Yong, C. Zhang, Z. Gu, J. Du, Z. Guo, X. Dong, J. Xie, G. Zhang, X. Liu, Y. Zhao, *ACS Nano* **2017**, *11*, 7164.
[50] S. Liu, T. H. Zeng, M. Hofmann, E. Burcombe, J. Wei, R. Jiang, J. Kong, Y. Chen, *ACS Nano* **2011**, *5*, 6971.
[51] A. Pompella, A. Visvikis, A. Paolicchi, V. D. Tata, A. F. Casini, *Biochem. Pharmacol.* **2003**, *66*, 1499.
[52] P. Kumar, K. Gill, S. Kumar, S. K. Ganguly, S. L. Jain, *J. Mol. Catal. A: Chem.* **2015**, *401*, 48.
[53] B. Ramalingam, T. Parandhaman, S. K. Das, *ACS Appl. Mater. Interfaces* **2016**, *8*, 4963.
[54] X. Chen, N. C. Berner, C. Backes, G. S. Duesberg, A. R. McDonald, *Angew. Chem., Int. Ed.* **2016**, *55*, 5803.
[55] H. Kojima, N. Nakatsubo, K. Kikuchi, S. Kawahara, Y. Kirino, H. Nagoshi, Y. Hirata, T. Nagano, *Anal. Chem.* **1998**, *70*, 2446.
[56] A. R. Collins, *Biochim. Biophys. Acta, Gen. Subj.* **2014**, *1840*, 794.
[57] B. M. Gyori, G. Venkatachalam, P. S. Thiagarajan, D. Hsu, M. V. Clement, *Redox Biol.* **2014**, *2*, 457.
[58] W. Yin, L. Yan, J. Yu, G. Tian, L. Zhou, X. Zheng, X. Zhang, Y. Yong, J. Li, Z. Gu, Y. Zhao, *ACS Nano* **2014**, *8*, 6922.
[59] J. Fan, N. He, Q. He, Y. Liu, Y. Ma, X. Fu, Y. Liu, P. Huang, X. Chen, *Nanoscale* **2015**, *7*, 20055.
[60] Z. Yao, X. Feng, C. Li, G. Shi, *Chem. Commun.* **2009**, 5886.
[61] E. J. Park, J. Yi, Y. Kim, K. Choi, K. Park, *Toxicol. In Vitro* **2010**, *24*, 872.